THE JOURNAL OF PHYSICAL CHEMISTRY B
A JOURNAL OF THE AMERICAN CHEMICAL SOCIETY

pubs.acs.org/JPCB

Article

Structure and Dynamics of Hydrofluorocarbon/Ionic Liquid Mixtures: An Experimental and Molecular Dynamics Study

Published as part of The Journal of Physical Chemistry virtual special issue "Doros N. Theodorou Festschrift".

Ning Wang, Yong Zhang, Karim S. Al-Barghouti, Rajkumar Kore, Aaron M. Scurto, and Edward J. Maginn*

Cite This: *J. Phys. Chem. B* 2022, 126, 8309−8321

Read Online

ACCESS | Metrics & More | Article Recommendations | Supporting Information

ABSTRACT: The physical properties of four ionic liquids (ILs), including 1-*n*-butyl-3-methylimidazolium tetrafluoroborate ([C_4C_1im][BF_4]), 1-*n*-butyl-3-methylimidazolium hexafluorophosphate ([C_4C_1im][PF_6]), 1-*n*-butyl-3-methylimidazolium thiocyanate ([C_4C_1im][SCN]), and 1-*n*-hexyl-3-methylimidazolium chloride ([C_6C_1im][Cl]), and their mixtures with hydrofluorocarbon (HFC) gases HFC-32 (CH_2F_2), HFC-125 (CHF_2CF_3), and HFC-410A, a 50/50 wt % mixture of HFC-32 and HFC-125, were studied using molecular dynamics (MD) simulation. Experiments were conducted to measure the density, self-diffusivity, and shear viscosity of HFC/[C_4C_1im][BF_4] system. Extensive analyses were carried out to understand the effect of IL structure on various properties of the HFC/IL mixtures. Density, diffusivity, and viscosity of the pure ILs were calculated and compared with experimental values. The good agreement between computed and experimental results suggests that the applied force fields are reliable. The calculated center of mass (COM) radial distribution functions (RDFs), partial RDFs, spatial distribution functions (SDFs), and coordination numbers (CNs) provide a sense of how the distribution of HFC changes in the liquid mixtures with IL structure. Detailed analysis reveals that selectivity toward HFC-32 and HFC-125 depends on both cation and anion. The molecular insight provided in the current work will help the design of optimal ILs for the separation of azeotropic HFC mixtures.

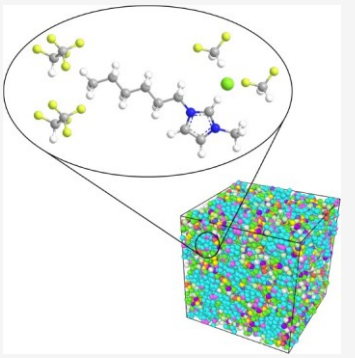

INTRODUCTION

Hydrofluorocarbon (HFC) refrigerants, known as third-generation refrigerants, are widely used in industrial, residential, and commercial cooling systems because of their zero ozone depleting potential. However, some HFC refrigerants have high global warming potential (GWP). For example, HFC-125 (CHF_2CF_3) in HFC-410A (GWP: 2088), the near-azeotropic mixture of HFC-32 (CH_2F_2) (GWP: 675) and HFC-125 (GWP: 3500), has a much higher GWP value than pure HFC-32.[1] It is, therefore, desirable to separate HFC-410A into its two components so that HFC-32 can be reused and HFC-125 repurposed. The Kigali Amendment,[2] signed in 2016 by 197 countries, mandates the phaseout of high GWP HFC refrigerants. Furthermore, on April 30, 2021, the US government proposed rules reducing the allowance of HFC production and consumption.[3] These announcements imposed a huge push to solve this important environmental problem. However, separating and recycling HFCs is difficult because many of them exist as azeotropic mixtures. Also, existing technology is infeasible due to high energy requirements or lack of separating agents. Promisingly, extensive publications have indicated that ionic liquids (ILs) can serve as an entrainer to efficiently perform azeotropic HFC separations.[4−7]

Shiflett and Yokozeki conducted systematic research on HFC-32 in 19 ILs, showed that the types of both cation and anion determine the solubility of HFC-32 in the ILs and, for the first time, indicated that HFC-32 has high solubility in ILs with fluorinated anions and low solubility in ILs with nonfluorinated anions.[8] The same authors also discovered large negative excess molar volumes in HFC-125 and 1-*n*-butyl-3-methylimidazolium hexafluorophosphate ([C_4C_1im][PF_6]) binary systems[9] implying strong interactions between HFC-125 and [C_4C_1im][PF_6] molecules. They also extensively investigated the diffusivity and solubility of various HFCs in two ILs, 1-*n*-butyl-3-methylimidazolium tetrafluoroborate ([C_4C_1im][BF_4]) and [C_4C_1im][PF_6], verified that there are large solubility differences among HFCs,[10] and suggested that [C_4C_1im][PF_6] is an efficient solvent to separate HFC-32 and HFC-125 via extractive distillation.[11] Lepre et al. measured HFC-134a (CF_3CH_2F) solubility in 1-ethyl-3-methylimidazo-

Received: August 12, 2022
Revised: September 23, 2022
Published: October 7, 2022

https://doi.org/10.1021/acs.jpcb.2c05787
J. Phys. Chem. B 2022, 126, 8309−8321

lium bis(trifluoromethylsulfonyl)imide ([C_2C_1im][TFSI]), 1-*n*-octyl-3-methylimidazolium bis(trifluoromethylsulfonyl)imide ([C_8C_1im][TFSI]), 1-(3,3,4,4,5,5,6,6,7,7,8,8,8-tridecafluorooctyl)-3-methylimidazolium bis(trifluoromethylsulfonyl)imide ([$C_8H_4F_{13}C_1$Im][TFSI]), 1-*n*-octyl-3-methylimidazolium bis(pentafluoroethylsulfonyl)imide ([C_8C_1im][BETI]), and 1-(3,3,4,4,5,5,6,6,7,7,8,8,8-tridecafluorooctyl)-3-methylimidazolium bis(pentafluoroethylsulfonyl)imide ([$C_8H_4F_{13}C_1$Im][BETI]) and found the solubility of HFC-134a follows the order of [C_2C_1im][TFSI] < [C_8C_1im][TFSI] < [C_8C_1im][BETI] < [$C_8H_4F_{13}C_1$Im][TFSI] < [$C_8H_4F_{13}C_1$Im][BETI].[12] They concluded that the fluorination of both the cation and the anion can increase solubility of HFC-134a with the effect of the cation being more significant. They also carried out molecular dynamics (MD) simulations to calculate radial distribution functions to better understand the solvation environment of HFC-134a in these five ILs. It was found that the anions favor the $-CH_2F$ site rather than the $-CF_3$ site in HFC-134a, while the terminal carbon of cations shows the opposite trend. In addition, HFC-134a was found to localize more around the terminal carbon of the cation alkyl chain than the imidazolium ring atoms. Dong et al. studied HFC-32 and HFC-152a (CH_3CHF_2) solubility in 1-ethyl-3-methylimidazolium trifluoromethanesulfonate ([C_2C_1im][OTf]) and 1-*n*-butyl-3-methylimidazolium trifluoromethanesulfonate ([C_4C_1im][OTf]) and proposed that the alkyl chain length of the cation can affect the solubility of these two HFCs: The longer the chain length, the higher the solubility.[13] Sosa and co-workers studied HFC-32, HFC-125, and HFC-134a and found that ILs with anions containing a fluorinated alkyl side chain with four carbon atoms like perfluoropentanoate ([$C_4F_9CO_2$]) and perfluorobutanesulfonate ([$C_4F_9SO_3$]) can improve the ideal selectivity of HFC-134a over HFC-32 in their binary mixtures, while fluoro-containing ILs without a fluorinated alkyl chain in the anions like triflate ([CF_3FO_3]) and bis(trifluoroethylsulfonyl)imide ($N(CF_3SO_2)_2$) are more selective toward HFC-32 over HFC-125 and toward HFC-134a over HFC-125.[14]

There are extensive molecular modeling works on HFCs[15−19] and ILs,[20−24] but little has been done on HFC/IL mixtures. Asensio-Delgado et al. applied the soft-SAFT equation of state and Aspen Plus simulator to model the separation of HFC-410A with ionic liquids.[25] They identified [C_2C_1im][TFSI] as the most promising candidate among three imidazolium ILs with fluorinated anions, 1-*n*-hexy1-3-methylimidazolium bis(trifluoromethylsulfonyl)imide ([C_6C_1im][TFSI]), [C_2C_1im][TFSI], and [C_4C_1im][PF_6]. They suggested that although these three ILs present no remarkable difference from a thermodynamic aspect, [C_2C_1im][TFSI] showed better performance in mass transfer due to its lower viscosity than the other two ILs. As far as we know, there have been no detailed molecular simulation studies of the structure and dynamics of HFC-32 and HFC-125 in ILs. The lack of molecular level explanation limits the understanding of how IL structure affects HFC separations.

A recent experimental work studied the refrigerants HFC-32 and HFC-125 in [C_4C_1im][BF_4], [C_4C_1im][PF_6], 1-*n*-butyl-3-methylimidazolium thiocyanate ([C_4C_1im][SCN]), 1-*n*-hexyl-3-methyl-imidazolium chloride ([C_6C_1im][Cl]), 1-*n*-butyl-3-methylimidazolium acetate ([C_4C_1im][C_1CO_2]), and 1-*n*-hexyl-3-methylimidazolium tris(pentafluoroethyl)trifluorophosphate ([C_6C_1im][FAP]) and demonstrated that HFC-32 has higher solubility in ILs with fluorinated anions ([BF_4], [PF_6], and [FAP]) than HFC-125 and that [C_4C_1im][SCN] has low absorption capacity for both HFC-32 and HFC-125.[26] It was also found that HFC-32 has higher diffusivity than HFC-125 in the binary mixtures, and the choice of IL significantly affects the solubility of HFCs, which provides a motivation for us to apply molecular modeling techniques along with experimental measurements to study these mixtures. In the current work, we performed MD simulations and experiments to study HFC-32 and HFC-125 in [C_4C_1im][BF_4]. We found that the simulations match the experimental data quite well. Based on this, we extended our simulation study to include HFC-32 and HFC-125 in [C_4C_1im][PF_6], [C_4C_1im][SCN], and [C_6C_1im][Cl]. We also studied the mixture of HFC-410A with all four ILs. Detailed chemical structures and shorthand names of the studied ILs and HFCs are given in Figure 1. We investigated density, diffusivity,

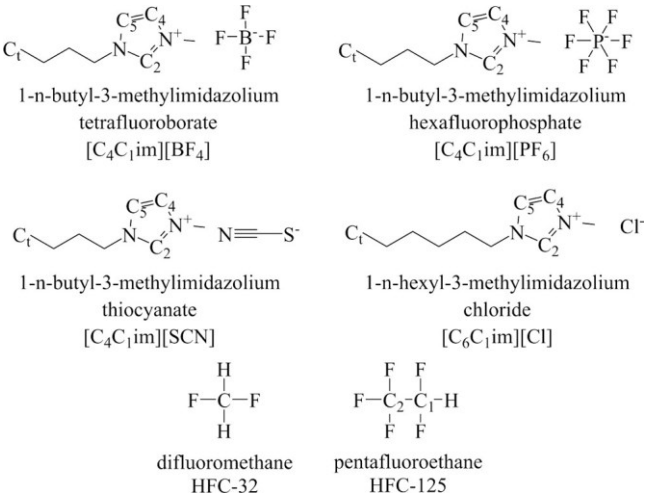

Figure 1. 2D chemical structures and shorthand names of ILs and HFC refrigerants.

viscosity, radial distribution functions (RDFs), and spatial distribution functions (SDFs). We verified the experimentally observed negative excess volume in HFC/IL mixtures and the diffusivity differences of HFC-32 and HFC-125 in the ILs. Finally, we discussed how IL structure plays a role in the solubility of HFCs in these ILs.

METHODS

Force Field. The general Amber force field (GAFF)[27] was applied to describe the bonded and nonbonded interactions of ILs. The functional form is

$$E = \sum_{\text{bonds}} k_r(r - r_0)^2 + \sum_{\text{angles}} k_\theta(\theta - \theta_0)^2 + \sum_{\text{torsions}} k_\phi \times [1 + \cos(n\phi - \gamma)] + \sum_{i=1}^{N-1}\sum_{j>i}^{N}\left\{4\varepsilon_{ij}\left[\left(\frac{\sigma_{ij}}{r_{ij}}\right)12 - \left(\frac{\sigma_{ij}}{r_{ij}}\right)^6\right] + \frac{q_i q_j}{4\pi\varepsilon_0 r_{ij}}\right\} \quad (1)$$

where k_r, k_θ, and k_ϕ are force constants; r_0, θ_0, and γ are nominal bond length, angle, and phase angle, respectively; n is periodicity; ε and σ are parameters for the Lennard-Jones (LJ) potential; q_i and q_j are partial charges to account for electrostatic interactions; and ε_0 is the vacuum dielectric

https://doi.org/10.1021/acs.jpcb.2c05787
J. Phys. Chem. B 2022, 126, 8309−8321

constant. Conventional dihedrals and improper dihedrals are all considered in the summation of torsions. Dihedral parameters that are not available in GAFF were fitted to quantum calculations at the B3LYP/6-311++g(d,p) level. The missing bond and angle parameters in GAFF for [BF_4] and [PF_6] were adapted from other works.[28,29] The [Cl] anion was described using the model from ref 30. For each isolated ion, structure optimization was carried out using the Gaussian 16 package[31] at the B3LYP/6-311++g(d,p) level. Partial charges were computed by fitting the electrostatic potential surface using the RESP method[32] and uniformly scaled by a factor of 0.8 to account for polarizability and charge transfer.[33] Force fields of HFCs were chosen and reproduced from one of the optimized parameter sets from ref 34. A complete listing of parameters is provided in Tables S1–S6.

Simulation Procedure. The LAMMPS package[35,36] was employed to perform MD simulations under isothermal–isobaric (NPT) and canonical (NVT) ensembles. The initial configuration was constructed using Packmol[37,38] by randomly inserting molecules into a cubic box. There were 400 ion pairs for each IL in all simulations and 30, 150, and 570 HFC molecules were added to the liquid phase resulting in the HFC mole fractions of 0.071, 0.272, and 0.588, respectively. These compositions correspond to experimentally determined state points of HFC-32 in [C_4C_1im][BF_4] from ref 10. Fewer data points were simulated for HFC-32 and HFC-125 in [C_4C_1im]-[SCN], HFC-125 in [C_4C_1im][BF_4], and HFC-125 in [C_4C_1im][PF_6] because these systems have lower solubility. Temperature and pressure for the pure IL simulations were set at 300 K and 1 atm, except for [C_6C_1im][Cl], where the conditions were 350 K and 1 atm. Temperatures, pressures, and HFC compositions for the HFC/IL binary and ternary systems are listed in Table 1. Periodic boundary conditions were applied in all directions. The time step was set to 1 fs and the cutoff of nonbonded interactions was 12 Å. A standard Ewald summation method[39] and a particle–particle particle–mesh method[40] with a precision of 0.0001 were used as long-range electrostatics solver for *NPT* and *NVT* simulations, respectively. For each system, an energy minimization for 10 000 iterations was first performed to reach a local energy minimum, which was followed by an *NPT* equilibration for 2 ns to reach the desired average volume. Density, isobaric expansivity, isothermal compressibility, and excess volume were computed from a 10 ns *NPT* production run, while self-diffusivity and structural properties were calculated from a 30 ns *NVT* production run. Shear viscosity was calculated from 30 independent 10 ns *NVT* production run following the 30 ns *NVT* production run mentioned before. Initial velocities were assigned randomly at the given temperature. The Nose–Hoover[41] thermostat and the extended Lagrangian[42] barostat were used to maintain the temperature and pressure, respectively. The nonbonded pairwise coefficients ε_{ij} and σ_{ij} for interactions between different atom types obey the Lorentz–Berthelot combining rules[43]

$$\varepsilon_{ij} = \sqrt{\varepsilon_{ii}\varepsilon_{jj}} \tag{2}$$

$$\sigma_{ij} = \frac{\sigma_{ii} + \sigma_{jj}}{2} \tag{3}$$

Property Calculations. Density was obtained from an *NPT* production run and block averaged over converged parts of the simulation. The uncertainty was estimated from the standard deviation, calculated as

$$\sigma = \sqrt{\frac{\sum_{i=1}^{n}\left(\bar{\rho}_i - \frac{\sum_{i=1}^{n}\bar{\rho}_i}{n}\right)^2}{n}} \tag{4}$$

where n is the number of blocks, and $\bar{\rho}_i$ is the average density of block i. Isobaric expansivity (α_P) and isothermal compressibility (κ_T) were calculated from the following thermodynamic expressions:

$$\alpha_P = V^{-1}(\partial V/\partial T)_P = -\rho^{-1}(\partial\rho/\partial T)_P = -(\partial \ln \rho/\partial T)_P \tag{5}$$

$$\kappa_T = -V^{-1}(\partial V/\partial P)_T = \rho^{-1}(\partial\rho/\partial P)_T = (\partial \ln \rho/\partial P)_T \tag{6}$$

The self-diffusivity was calculated from the following Einstein equation[44] using the PyLAT package:[45]

$$D_s = \frac{1}{6}\lim_{t\to\infty}\frac{\mathrm{d}}{\mathrm{d}t}\langle[\mathbf{r}(t) - \mathbf{r}(0)]^2\rangle \tag{7}$$

where $\langle[r(t) - r(0)]^2\rangle$ is the mean-squared displacement (MSD) whose formula is

$$\langle[\mathbf{r}(t) - \mathbf{r}(0)]^2\rangle = \frac{1}{n+1}\sum_{t_0=0}^{n}\frac{1}{N}\sum_{i=1}^{N}[\mathbf{r}_i(t_0 + t) - \mathbf{r}_i(t_0)]^2 \tag{8}$$

r_i is the position of the center of mass (COM) of molecule i, N is the number of molecules, t_0 are different time origins, $n + 1$ is the number of time origins used, and the angle bracket denotes an ensemble average. A system-size correction was applied to simulated self-diffusivity values of pure ILs according to the approach of Yeh and Hummer[46] using the calculated viscosity.

Table 1. Detailed Simulation Temperatures, Pressures, and Corresponding HFC Composition for HFC/IL Binary and Ternary Systems

	T (K)	P (atm)	x
	298.2	0.984	0.071
HFC-32 in [C_4C_1im][BF_4]	298.2	3.95	0.272
	298.2	9.868	0.588
	298.2	0.92	0.071
HFC-32 in [C_4C_1im][PF_6]	298.2	3.95	0.272
	298.2	10.22	0.588
HFC-32 in [C_4C_1im][SCN]	298.2	2.45	0.071
	298.2	7.57	0.272
HFC-32 in [C_6C_1im][Cl]	298.2	1.55	0.071
	298.2	5.94	0.272
	298.2	16.44	0.588
HFC-125 in [C_4C_1im][BF_4]	298.2	3	0.071
	298.2	8.1	0.272
HFC-125 in [C_4C_1im][PF_6]	298.2	2.9	0.071
	298.2	8.87	0.272
HFC-125 in [C_4C_1im][SCN]	298.2	7.382	0.071
	298.2	0.84	0.071
HFC-125 in [C_6C_1im][Cl]	298.2	3.7	0.272
	298.2	8.72	0.588
HFC-410A in [C_4C_1im][BF_4]	298.2	0.984	0.177
HFC-410A in [C_4C_1im][PF_6]	298.2	0.984	0.177
HFC-410A in [C_4C_1im][SCN]	298.2	0.984	0.177
HFC-410A in [C_6C_1im][Cl]	298.2	0.984	0.177

https://doi.org/10.1021/acs.jpcb.2c05787
J. Phys. Chem. B 2022, 126, 8309–8321

The shear viscosity was calculated using a time decomposition method[47] applying the Green–Kubo equation to each trajectory

$$\eta = \frac{V}{6k_B T} \sum_{\alpha \le \beta} \int_0^\infty \langle \bar{P}_{\alpha\beta}(t) \cdot \bar{P}_{\alpha\beta}(0) \rangle \, dt \tag{9}$$

where V is the box volume, T is the temperature, k_B is the Boltzmann constant, and $P_{\alpha\beta}$ is the modified pressure tensor. The standard deviation and average over 30 trajectories as a function of time were calculated and fit to a power law function and a double exponential function, respectively. Modified pressure tensors conform to the following rules: $P_{xy} = P_{xy}$, $P_{yz} = P_{yz}$, $P_{xz} = P_{xz}$, $P_{xx} = 0.5(P_{xx} - P_{yy})$, $P_{yy} = 0.5(P_{yy} - P_{zz})$, and $P_{zz} = 0.5(P_{xx} - P_{zz})$. A bootstrapping method was utilized to estimate the standard deviation of the calculated viscosity,[48] which was taken as the uncertainty.

The liquid structure was studied in terms of RDF

$$g_{ij}(r) = \frac{V}{N_i N_j} \sum_{i=1}^{N_i} \sum_{j=1}^{N_j} \delta(r - r_{ij}) \tag{10}$$

where N_i and N_j are the numbers of particles i and j, r_{ij} is the distance between particles i and j, and $\delta(r - r_{ij})$ is the Dirac function. Coordination number of species j around species i was computed according to the following formula

$$\mathrm{CN}_{ij}(r') = \frac{N_j}{V} \int_0^{r'} g_{ij}(r) \, dr \tag{11}$$

where r' is the cutoff distance. SDF is another way to present the liquid structure which was calculated similarly to RDF but in a 3D manner.

Experimental Methodology. *Vapor–Liquid Equilibrium, Density, and Viscosity.* A multifunctional apparatus was utilized to measure the gas solubility, density and shear viscosity. A detailed description of the apparatus and its operation will be provided in an upcoming publication. An overview will be given here. A high-pressure viscometer and high-pressure densitometer were combined in series with a view cell similar to a Jurgenson cell. The working apparatus was heated in an ESPEC climate-control chamber (model BTZ-475) with a temperature range of −70 to 180 °C with an approximate ±0.2 °C control. A given amount of ionic liquid was initially introduced to the system and dried again at elevated temperatures and vacuum pressures (~2 mbar). A measured mass quantity of the gas was introduced and mixing of the components was performed by circulating the liquid using an Eldex reciprocating piston pump (model Optos 2HM) that drew the liquid from the bottom of the view cell, circulated it through the densitometer and viscometer in series, and re-entered the view cell where the liquid droplets fell through the vapor phase back to the liquid phase. At each pressure, the system was circulated for approximately 1 h (at flow rates ranging between 5 and 30 mL/min) to reach phase equilibrium. Gas solubility measurements were obtained from a mass balance method knowing the mass of IL and gas introduced to the system, the liquid density, and the total volume of the system including lines. The uncertainty of the gas solubility measurements was nominally ±0.005 mole fraction but whose uncertainty was calculated for each individual point. The temperature of the system was measured with a Pt100 RTD with an uncertainty of ±0.1 °C. The pressure was measured using an OMEGA digital pressure gauge (model PX309–500AI) with a 34.47 bar maximum limit and an uncertainty of 0.25% full scale (±0.09 bar).

Viscosity was measured with a modified Cambridge Applied Systems (Currently: Cambridge Viscosity, a unit of Petroleum Analyzer Company) ViscoPro 2000, 4-SPL-440 high-pressure viscometer. The viscometer measurements are based on the principle of annular fluid flow around an axially oscillating piston in a cylindrical chamber.[49] A controlled magnetic field oscillates a piston a certain distance and the time of travel is correlated to the viscosity of the fluid sample. The measuring system is capable of 190 °C and 1379 bar with viscosities ranging from 0.2 to 10 000 cP. The nominal viscosity accuracy is reported as ±1% full scale of the viscosity range of the specific piston installed. However, better results are often achieved in practice with a run-to-run repeatability of about ±0.5%. Each reported viscosity measurement is the average of 10 measurements with its standard deviation. A detailed description of the device is reported elsewhere.[50]

Density measurements were conducted using an Anton Paar DMA HPM external measuring unit capable of pressures up to 1400 bar and temperatures up to 200 °C. The measuring unit employs the principle of a vibrating U-tube densitometer in which the vibration frequency of a vibrating U-tube filled with a fluid of interest is measured and correlated to the period of oscillation. The period of oscillation, temperature, and pressure are relayed to a mPDS 5 evaluation unit where they are fit to a conversion polynomial that correlates the measured variables to density. The density is corrected for minor viscosity effects using a factory-supplied calibration. The densitometer unit includes a temperature sensor with a reported uncertainty of <0.1 °C. Density measurements have an estimated overall accuracy of ±0.15%. Further information on the aforementioned polynomial and evaluation unit operation is provided elsewhere.[51]

Diffusivity. The self-diffusivity of the IL cation and anion, and the dissolved gas were measured by following our previously reported NMR procedure.[52] Typically, ^{1}H and ^{19}F NMR was used here to determine the self-diffusion of both the cation and anion of IL and the dissolved refrigerant gas. A Bruker 500 MHz NMR instrument was used to measure the translational diffusion with a pulsed-field gradient (PFG) method. In a PFG, the reduction of a signal intensity resulting from the combination of molecular diffusion and magnetic force gradient pulses on nuclear spins can be measured. The reduction of the signal intensity is based on the diffusion time as well as the gradient parameters: gradient strength and length of gradient. The intensities for the sample are given by the following equation:[53]

$$\ln\left(\frac{I}{I^\circ}\right) = -(\gamma \delta g)^2 D\left(\Delta - \frac{\delta}{3} - \frac{\tau}{2}\right) \tag{12}$$

where g is the gradient strength (G/m), I is the integral value at given g, I° is integral value at given $g = 0$, γ is the gyromagnetic ratio in G/s (26752 for ^{1}H NMR and 25182 for ^{19}F NMR), δ is the length of gradient pulse in s ($p30 \times 2$)), Δ is the diffusion time in s, τ is the delay for refocusing in s, and D is the diffusion coefficient (m^2/s). A more detailed description of the NMR method used for diffusion is discussed elsewhere.[54,55]

To measure the diffusion coefficient of molecules of a liquid mixed with a compressed gas, a medium pressure NMR tube from Wilmad Lab Glass (Model PV-ANV Pressure/Vacuum

https://doi.org/10.1021/acs.jpcb.2c05787
J. Phys. Chem. B 2022, 126, 8309−8321

NMR Valve) which is capable of pressures to 13 bar was used. Under N_2 in a glovebox, the IL sample was injected into the tube to the height of ~3 cm. The valve assembly was connected to the NMR tube. The NMR tube was then removed from the glovebox and connected to the pressure gauge (through a 5 ft. 1/16 in. PEEK tube) and followed by gas cylinder. Before injecting refrigerant gas into the IL, the system was degassed for 1 h under vacuum. Later, the vacuum line was closed and a certain amount of gas was injected. The tube was rocked back and forth to increase mixing and reduce the time to equilibrium. After several hours, the NMR tube was placed in the temperature controlled chiller (at 25 °C) for a couple of days. The NMR tube was placed within the NMR instrument for 2 h to avoid any temperature differences, and the NMR tube pressure was monitored to ensure that the pressure remained constant.

RESULTS AND DISCUSSIONS

Properties of Pure ILs. *Density.* To validate the force fields, the properties of the pure ILs were studied first. As an initial test, the density as a function of temperature and pressure was calculated for the pure ILs. The results are plotted in Figure 2 and compared with available experimental results.

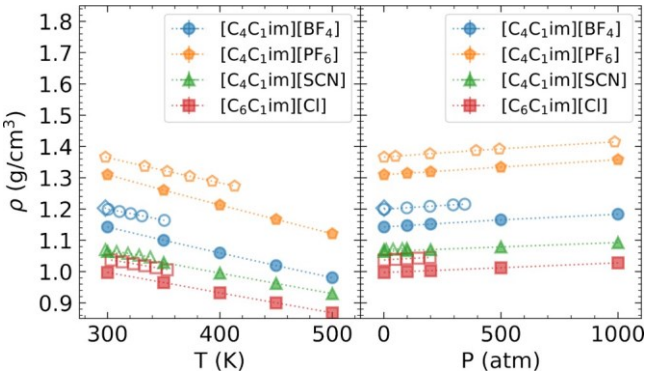

Figure 2. Density of pure $[C_4C_1im][BF_4]$ (blue), $[C_4C_1im][PF_6]$ (orange), $[C_4C_1im][SCN]$ (green), and $[C_6C_1im][Cl]$ (red) as a function of temperature (left) at 1 atm for the simulations and similar pressures for experiments (0.997 atm for $[C_4C_1im][PF_6]$ and 0.987 atm for the rest), and as a function of pressure (right) at 300 K for the simulations and at 298.15 K for experiment (blue diamond) in this work, and similar temperatures for experiments in literature (300.65 K for $[C_4C_1im][BF_4]$, 298.15 K for $[C_4C_1im][PF_6]$ and $[C_4C_1im]$-$[SCN]$, and 303.15 K for $[C_6C_1im][Cl]$). Simulation results are in filled symbols whereas experimental data are in open symbols. The estimated error bars are smaller than the symbols.

Both calculated and experimental[56−59] density values are summarized in Table S7. Deviation among different experimental data for the same IL is within 0.1%. As shown in the figure, the density decreases with increasing temperature and increases with increasing pressure, and all follow linear relations. The averaged deviation between simulation and experiment is summarized in Table S7 and was calculated as $\frac{1}{N}\sum_N \frac{\rho_{sim.}-\rho_{expt.}}{\rho_{expt.}}$, where N is the number of state points, $\rho_{sim.}$ is the simulated density, and $\rho_{expt.}$ is the experimental density. Each state point at experimental condition was estimated based on a linear fit of the simulation results. The MD simulations slightly underpredict the density. The maximum averaged deviation was found to be around −5.1%. As shown in Figure 2, MD simulations perfectly capture the relative order of density: $[C_4C_1im][PF_6]$ > $[C_4C_1im][BF_4]$ > $[C_4C_1im][SCN]$ > $[C_6C_1im][Cl]$. The temperature and pressure dependence of the density is captured as demonstrated by the isobaric expansivity α_P and isothermal compressibility κ_T values shown in Table S8.

Self-Diffusivity. Based on the Einstein relation (eq 7), the self-diffusion coefficients of the cations and anions at 300 K (350 K for $[C_6C_1im][Cl]$) and 1 atm were derived from the diffusive region of the calculated MSD. The results are shown in Figure 3 and compared with available experimental results.

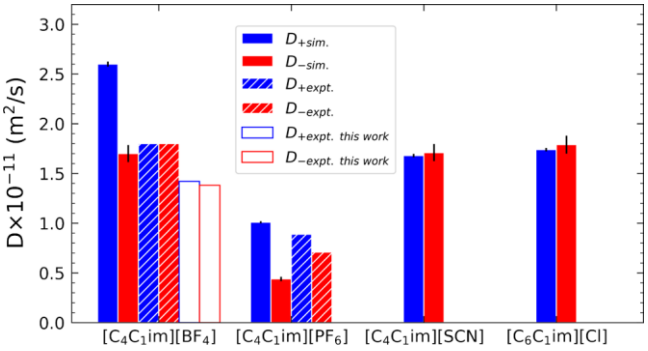

Figure 3. Self-diffusivity of pure ILs at 300 K and 1 atm except for $[C_6C_1im][Cl]$ which is at 350 K and 1 atm compared with experiment in this work (open) at 298.15 K and in literature[60] (hatched pattern).

We also report our experimental diffusivities for $[C_4C_1im][BF_4]$, which are slightly lower than previous experimental measurements. For all the ILs studied in the current work, the calculated diffusivity of the cations is higher than or close to that of the corresponding anions, although the anions are smaller than the cations in all ILs. Compared with experiments,[60] MD simulations overestimate the cation diffusivity and underestimate the anion diffusivity for both $[C_4C_1im][BF_4]$ and $[C_4C_1im][PF_6]$. In addition, the simulations predict that the cation diffusivity is larger than the anion diffusivity, which is not observed experimentally. However, the trend that $[C_4C_1im][BF_4]$ tends to have faster dynamics than $[C_4C_1im][PF_6]$ was captured by the simulations. No experimental data were found for the other two ILs. Overall, the calculated self-diffusivities show reasonable agreement with experimental results. Table S9 provides a summary of the calculated and experimental diffusivity values from literature, and Table S10 provides experimental diffusivity values measured in this work.

Shear Viscosity. The calculated shear viscosities for the pure ILs are shown in Figure 4 and compared to experimental results. All simulations were done at 300 K except for $[C_6C_1im][Cl]$ which was calculated at an elevated temperature of 350 K due to its high viscosity at 300 K. For each IL, multiple experimental results were found in the literature which deviate from each other significantly in some cases. Experimental values at simulation temperatures were estimated from the Vogel−Fulcher−Tammann equation and are summarized in Table S11. For a comprehensive comparison, the average and standard deviation of experimental results for a given IL were computed and plotted with simulation values in Figure 4. As shown in the figure, for two of the four ILs studied in the current work, $[C_4C_1im][BF_4]$ and $[C_4C_1im][PF_6]$, the simulated viscosities agree with experimental values very well. Our experimental results for $[C_4C_1im][BF_4]$ also agree well with previous experiments. For the other two ILs, simulation

https://doi.org/10.1021/acs.jpcb.2c05787
J. Phys. Chem. B 2022, 126, 8309−8321

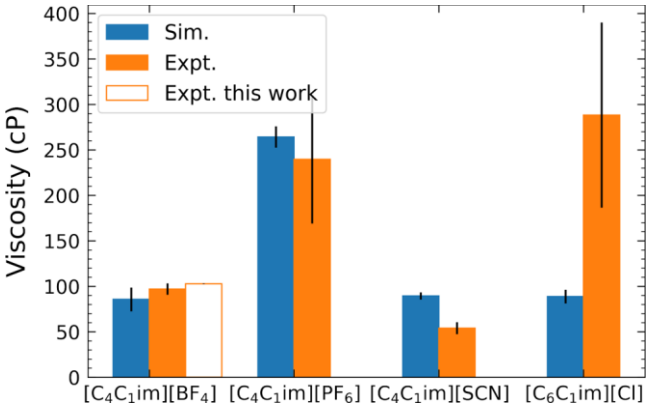

Figure 4. Shear viscosity of pure ILs simulated at 300 K and 1 atm except for [C_6C_1im][Cl] which was simulated at 350 K and 1 atm. The average and the corresponding standard deviation from multiple experimental results interpolated at simulation temperature are included for comparison. All the data are summarized in Table S11. Experimental (unfilled orange bar) viscosity of [C_4C_1im][BF_4] measured at 298.15 K in the present work is also shown, with the value documented in Table S12.

significantly underestimates the viscosity of [C_6C_1im][Cl] and slightly overestimates that of [C_4C_1im][SCN]. Aside from the [C_6C_1im][Cl] result and considering that the viscosity is a property that is hard to predict accurately for ILs, the agreement between simulation and experiments presented here is reasonable. The results suggest that the model for [Cl] needs refinement.

Overall, the applied force fields in the current work can predict both the density and the dynamics reasonably well for the studied ILs. The force field parameters for the HFCs were already carefully validated previously.[34] The mixtures of the ILs and HFCs were studied next.

HFC/IL Mixtures. *Density and Excess Volume.* The experimentally measured and simulated mass density for both HFC/IL systems are illustrated in Figure 5, and the

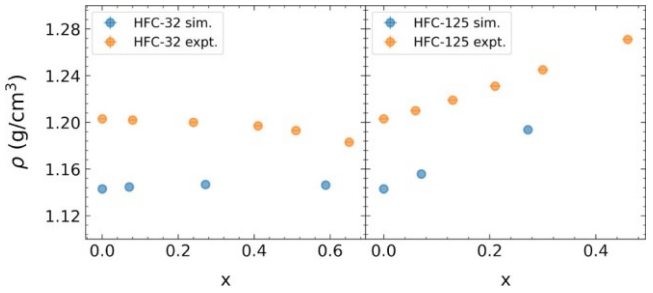

Figure 5. Experimental (orange) and simulated (blue) density ρ as a function of HFC mole fraction x for the mixtures of [C_4C_1im][BF_4] with HFC-32 (left) and HFC-125 (right), respectively. The estimated error bars are smaller than the symbols.

data are reported in Tables S12 and S13. The mass density of the HFC-125/IL system exhibits an increase with increased molar composition of the dissolved gas, while the HFC-32/IL system exhibits a gradual decrease in density across the composition regime investigated. The decrease in density for the HFC-32/IL system at a dissolved HFC-32 molar composition of 0.65 compared to the pure IL density is 1.7%. The increase in density for the HFC-125/IL system at a dissolved HFC-125 molar composition of 0.46 relative to the pure IL density is 5.6%. Pure component HFC-125 has a saturated liquid mass density of 1.189 g/cm^3 with a density to pressure sensitivity, $\frac{\partial\rho}{\partial P}$, of 0.0015 g/cm^3·bar.[61,62] If the density of the dissolved HFC-125 in the mixture is assumed to have a similar dependency on pressure, the density of the pure component would not be expected to have comparable density values as that of the IL until higher pressures (compositions; > 20 bar) are achieved. The IL density also has a slight dependency on pressure within the pressure regimes investigated ($\frac{\partial\rho}{\partial P}$ = 0.0005 g/cm^3·bar per data reported by Matkowska et al.).[63] Hence, the increase in density cannot be explicitly attributed to potential hydrostatic pressure effects, but effects due to composition and intermolecular interactions.

The simulated density of the HFC and IL binary mixtures were calculated from MD simulations, and the results with corresponding standard deviation are summarized in Table S13. From Figure 5, the simulated density of HFC-32/[C_4C_1im][BF_4] shows a slight increase followed by a slight decrease with increasing HFC-32 mole fraction, while the simulated density of HFC-125/[C_4C_1im][BF_4] shows a steady increase with increasing HFC-125 mole fraction, which is consistent with experiments. Simulations of both systems consistently underestimate density by less than 5%, which is similar to what was observed for the pure IL.

The simulated excess mixing volume ΔV was calculated as

$$\Delta V = V_{\text{mix}} - V_{\text{ideal}} \tag{13}$$

where V_{mix} is the actual molar volume of the mixture from the simulations and V_{ideal} is the molar volume of the mixture under the ideal mixing assumption

$$V_{\text{ideal}} = xV_{\text{HFC}} + (1 - x)V_{\text{IL}} \tag{14}$$

where x is the mole fraction of HFC, V_{HFC} is the molar volume of pure HFC at the saturation pressure that corresponds to the system temperature, and V_{IL} is the molar volume of the pure IL at the same temperature. The calculated relative excess mixing volumes ($\Delta V/V_{\text{ideal}}$) are shown in Figure 6 for mixtures of ILs with HFC-32 and HFC-125, respectively. There are fewer data points for HFC-32 and HFC-125 in [C_4C_1im][SCN], HFC-125 in [C_4C_1im][BF_4], and HFC-125 in [C_4C_1im][PF_6] because these systems have lower solubility. As shown in the figure, the mixing of HFCs with ILs is not ideal, and a negative excess volume is observed for all the mixtures, suggesting that

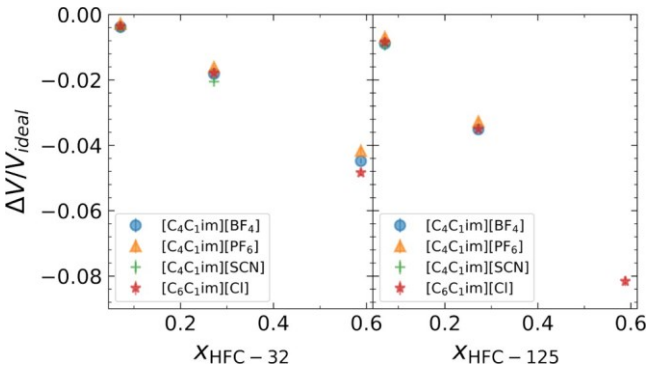

Figure 6. Calculated relative excess volume ($\Delta V/V_{\text{ideal}}$) as a function of HFC fraction for the mixtures of ILs with HFC-32 (left) and HFC-125 (right), respectively. The estimated error bars are smaller than the symbols.

https://doi.org/10.1021/acs.jpcb.2c05787
J. Phys. Chem. B 2022, 126, 8309−8321

the HFCs can find free space among the IL molecules, therefore making the mixture volume smaller than expected by assuming ideal mixing. HFC-125 has larger excess volumes in the studied ILs than HFC-32. For both HFCs, the excess volume increases (more negative) as the HFC mole fraction increases. On the other hand, the excess volumes are the same for a given HFC at the same mole fraction in all ILs except for HFC-32 at the highest concentration. For the mixtures with the highest HFC-32 concentration, the absolute value of the excess volume follows the order $[C_6C_1im][Cl] > [C_4C_1im][BF_4] > [C_4C_1im][PF_6]$. Detailed values of the calculated excess volumes are documented in Table S13.

Self-Diffusivity. The self-diffusion coefficients for binary mixtures of $[C_4C_1im][BF_4]$ and HFC-32 or HFC-125 were measured at 298.15 K and various pressures using an ^1H and ^{19}F NMR methods for the cation and anion, respectively. The data are provided in Table S10. The self-diffusivity of pure $[C_4C_1im][BF_4]$ IL (both cation as well as anion) was measured at 298.15 K and ambient pressure and compared with literature data.[64] The measured self-diffusion coefficient of the cation $[C_4C_1im]$ and anion $[BF_4]$ were 1.42×10^{-11} and 1.38×10^{-11} m²/s respectively and compare well with the literature values of 1.45×10^{-11} m²/s ($[C_4C_1im]$) and 1.34×10^{-11} m²/s ($[BF_4]$).[64]

The self-diffusivities of the $[C_4C_1im][BF_4]$ IL saturated with compressed HFC gas (HFC-125 or HFC-32) were measured at the same temperatures and pressures as the simulation data, and results are summarized in Figure 7 and Table S10. Similar to the viscosity measurements, vapor−liquid equilibrium data were interpolated to calculate the compositions at the measured diffusivities. With increasing mole fraction of either of the HFC gases, the self-diffusivities of the cation, anion, and HFC gas were significantly increased (see Figure 7). Generally, the diffusivity of the cations and anions are similar whether in the pure IL or the HFC mixture. While the cations may diffuse slightly faster than the anions for the pure IL, the anions may diffuse faster at high concentration of the dissolved HFC. The HFC-32/$[C_4C_1im][BF_4]$ system showed higher diffusivities than in the HFC-125/$[C_4C_1im][BF_4]$ system at similar compositions. Based on PFG-NMR data, the following general diffusivity trend has been confirmed at our investigated condition: HFCs > $[BF_4]$ > $[C_4C_1im]$. No direct comparisons of self-diffusivity are available in the literature for ionic liquids with compressed HFC-125/HFC-32. One of the authors has measured the self-diffusivity of $[C_6C_1im][TFSI]$ IL cation with HFC-134a using ^1H NMR.[52] At 298.15 K and a pressure of 4.2 bar (~55% mole composition of HFC-134a), the diffusivity of the cation $[C_6C_1im]$ was 2.55×10^{-11} m²/s, while here with the smaller cation and anion for $[C_4C_1im][BF_4]$ at 55% mole of HFC-32, the cation diffusivity is 19.7×10^{-11} m²/s.

The diffusivity results obtained from MD simulations in different ILs as a function of HFC-32 or HFC-125 mole fraction are shown in Figure 7 and Table S14. Since the viscosity calculations are expensive and we are only interested in the diffusivity trend, the system size correction was not applied to HFC/IL mixtures. However, based on the system-size corrections for pure ILs, we expect the correction to be 5–11%. Uncertainty analysis was performed for the HFC-125 in $[C_4C_1im][BF_4]$ at the lowest concentration system based on three independent simulations. The standard deviation for each species was calculated using

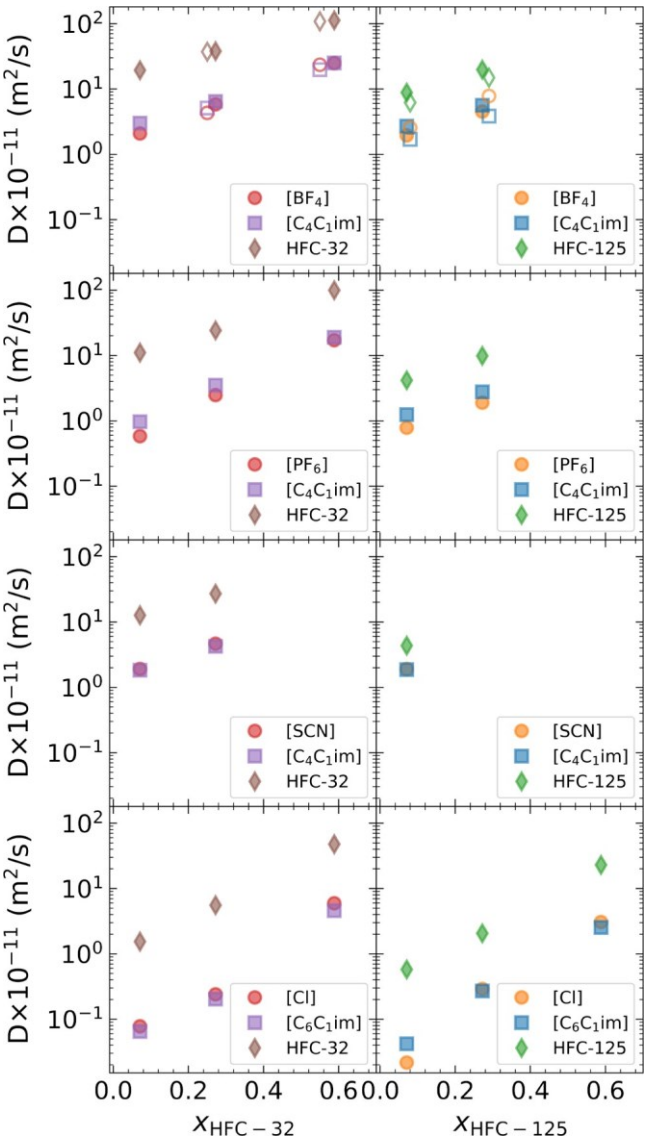

Figure 7. Calculated (filled) and measured (open) self-diffusion coefficients for the binary mixtures of HFC-32 (left) and HFC-125 (right) in $[C_4C_1im][BF_4]$ (first row), $[C_4C_1im][PF_6]$ (second row), $[C_4C_1im][SCN]$ (third row), and $[C_6C_1im][Cl]$ (last row), respectively. The estimated error bars are smaller than the symbols and not shown in the plots.

$$\sigma = \sqrt{\frac{\sum_{i=1}^{n} (D_i - \bar{D})^2}{n}} \quad (15)$$

where n is 3, the number of independent simulations conducted; D_i is the diffusivity result from one simulation; and $\bar{D}$ is the average of diffusivity values over n simulations. The relative uncertainty $\delta = \sigma/\bar{D}$ was found to be 0.07, 0.06, and 0.25 for the cation, anion and HFC, respectively, as shown in Table S15. To save CPU time, the same δ was assumed for all the binary mixtures studied in the current work. As shown in Figure 7, with increasing HFC mole fraction, diffusivities of all species increase for mixtures of both HFCs. Diffusivities of HFCs are around a factor of 2–27 greater than those of the ILs with the actual ratio varying depending on the HFC and IL. HFC-125 diffuses slower than HFC-32 due to the relatively larger size of HFC-125 compared to HFC-32, which is consistent with experimental observations.[26] In the binary

https://doi.org/10.1021/acs.jpcb.2c05787
J. Phys. Chem. B 2022, 126, 8309−8321

mixtures of HFC in [C_4C_1im][BF_4] and [C_4C_1im][PF_6], the cation diffusivity is higher than that of the anion in [C_4C_1im][BF_4] and [C_4C_1im][PF_6]. However, the diffusivities are similar for the cation and the anion in [C_4C_1im][SCN] and high HFC fractions in [C_6C_1im][Cl]. These behaviors are similar to those observed in the pure ILs. The only exception is the HFC-125 mixture in [C_6C_1im][Cl] at the lowest HFC-125 fraction, in which the diffusivity of the [C_6C_1im] was found to be slightly higher than that of the [Cl]. Overall, the calculated diffusivities of the HFC/[C_4C_1im][BF_4] systems agree extremely well with our experiments. These results suggest that the addition of HFC does not change the relative dynamics of the cations and anions significantly, although the pressures are different.

Shear Viscosity. The experimental and simulated shear viscosity of [C_4C_1im][BF_4] as a function of mole fraction of saturated HFC-32 and HFC-125 are shown in Figure 8; a

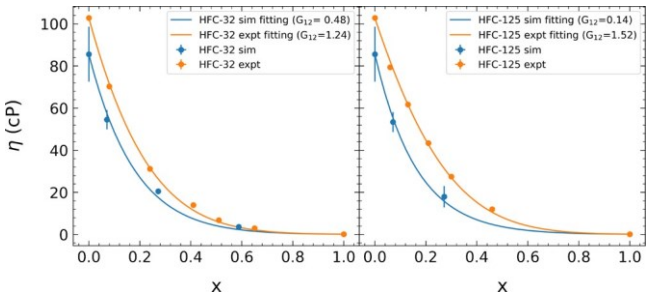

Figure 8. Simulated and experimental shear viscosity for the binary mixtures of HFC-32 (left) and HFC-125 (right) in [C_4C_1im][BF_4], respectively. Dots are real state points obtained from simulation or experiment, and the solid line is the fitting curve.

listing of all experimental values are given in Table S12. Vapor–liquid equilibrium was measured simultaneously with the viscosity and density data. Both HFCs are very soluble in the ionic liquid. The solubility data reported in Table S12 have a percent average absolute relative deviation (%AARD) of 4.1% for the HFC-32 system relative to interpolated literature data in a similar range of pressure[10] and 3.8% for the HFC-125 system.[26] From the vapor–liquid equilibrium data measured here for each of the systems, the compositions are interpolated at the conditions of the viscosity measurement and are used in Figure 8 and Table S12. The viscosity significantly decreases with increasing HFC composition for both gases across the composition regimes investigated. The viscosity decreases relatively linearly with composition of either HFC to approximately 30% mole of the dissolved gas. Beyond this composition, the linearity changes slightly. The percent decrease in liquid viscosity at a HFC-32 molar composition of 0.51 in the liquid mixture is 93% from pure [C_4C_1im][BF_4]. Similarly, the percent decrease in viscosity at a HFC-125 molar composition of 0.46 in the liquid mixture is 88%.

No data have been reported on the viscosity of [C_4C_1im][BF_4] and these HFC gases in the literature. However, the viscosity of [C_6C_1im][TFSI] saturated with the HFC gas HFC-134a (one fluorine less than HFC-125) has been reported.[52] In addition, we have reported on the viscosity of CO_2-saturated [C_6C_1im][TFSI].[65] Similar to what is obtained in the current work, there is a large decrease in viscosity with pressure/composition of the gas for this system. Zhang et al. measured the viscosity of [C_6C_1im][TFSI] saturated with the HFC gas 1,1-difluoroethane (HFC-152a) as well as [C_6C_1im][TFSI] saturated with the hydrofluoroolefins *trans*-1,3,3,3-tetrafluoropropene and 2,3,3,3-tetrafluoroprop-1-ene (R1234ze(E) and R1234yf).[66,67] Tomida et al. measured the viscosity of [C_4C_1im][BF_4] subsaturated with CO_2 at various compositions and elevated pressures.[68] The CO_2/[C_4C_1im][BF_4] system exhibits a similar decrease in viscosity with increasing dissolved gas composition as the HFC-32 and HFC-125 saturated [C_4C_1im][BF_4] systems investigated here. The viscosity decrease in all of the [C_4C_1im][BF_4] systems is evidently steeper than the viscosity decrease exhibited in any of the [C_6C_1im][TFSI] systems.

The simulated shear viscosities of binary mixtures of HFC-32 and HFC-125 in [C_4C_1im][BF_4] are plotted along with experimental data in Figure 8. Numerical values from simulations are documented in Table S16. The simulations agree reasonably well with the experimental data, though they systematically underestimate absolute values. They capture the trend of decreasing viscosity with increasing mole fraction of HFC. This can be explained by the dilution effect that adding relatively low viscosity HFC to high viscosity IL will make the mixture viscosity lower. The simulation and experimental viscosity data were fit to an empirical model[69]

$$\ln \eta_{\text{mixture}} = x_1 \ln \eta_1 + x_2 \ln \eta_2 + 2x_1x_2G_{12} \qquad (16)$$

where x_1 and x_2 are the mole fraction of HFC and IL in the mixture, respectively, η is the viscosity, and G_{12} is a parameter to reflect nonideality. When $G_{12} = 0$, it indicates ideal mixing, while larger values of G_{12} indicate greater deviation from ideality. As shown in Figure 8, both simulations and experiment show positive deviations from ideality ($G_{12} > 0$), but the simulations predict a smaller deviation from ideality than experiment. Overall, the simulations agree with the experimental data reasonably well.

Liquid Structure. COM RDF. The liquid structures in the binary mixtures of HFC in ILs were studied in terms of the COM RDFs. Results for HFC-32 and HFC-125 in [C_6C_1im][Cl] are shown in Figure 9; RDFs for other systems are shown

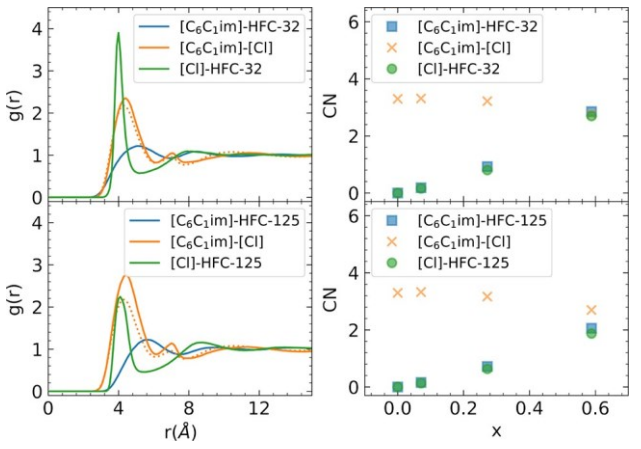

Figure 9. Left: Calculated COM RDFs in the binary mixtures of HFC-32 (top) and HFC-125 (bottom) in [C_6C_1im][Cl] at HFC mole fractions of 0 (dotted line) and 0.588 (solid line). Right: Calculated coordination numbers (CN) for the same mixtures with a cutoff distance of 6.1 Å (the distance corresponding to the first solvation shell of [C_6C_1im]–[Cl] interaction defined by the distance of the first minimum between the first two maxima in the [C_6C_1im]–[Cl] RDF).

https://doi.org/10.1021/acs.jpcb.2c05787
J. Phys. Chem. B 2022, 126, 8309−8321

in Figure S1. The typical charge alternating structure is observed in each system, with an initial sharp peak at short distance, corresponding to cation–anion interactions. This is followed by weaker peaks at longer distances, corresponding to cation–cation and anion–anion interactions. For the studied binary mixtures, the cation–cation, cation–anion, and anion–anion RDFs change very little with HFC concentrations for HFC-32 in all ILs and HFC-125 in [C_4C_1im][BF_4], [C_4C_1im][PF_6], and [C_4C_1im][SCN]. However, the cation–anion RDF of HFC-125 in [C_6C_1im][Cl] binary mixtures shows a slight increase in peak height at the highest HFC-125 composition. This RDF at the highest HFC-125 composition is shown in Figure 9. The results for HFC-32 in [C_6C_1im][Cl] are also included for comparison.

The coordination number (CN) between the cation and anion as a function of HFC-125 composition was calculated for these mixtures, and the results are shown in Figure 9. With increasing concentration of HFC, the [C_6C_1im]–[Cl] CN decreases slightly from 3.3 in pure IL to 2.7 when the HFC-125 mole fraction is 0.588. Similar behavior was observed for HFC-32 in [C_6C_1im][Cl] mixtures. These results show that the addition of HFCs does not significantly affect the IL packing structure in the liquid phase, even at these high concentrations. The slight increase in the peak height in [C_6C_1im][Cl] mixture with HFC-125 is likely due to the decrease of the average number density of the cation and anion used to normalize the RDF (see eq 10). The increase in peak height was not observed in other HFC-125 mixtures because of lower HFC concentrations. It was not observed for HFC-32 mixtures due to its small size. The RDFs and CNs of HFC surrounding the cation and anion were also calculated and are included in Figure 9. For a fair comparison, the same cutoff distance of 6.1 Å as for cation–anion interaction was used. With increasing HFC concentrations, the CNs of HFC surrounding cation and anion increase in a similar manner. At 0.588 HFC mole fraction, each cation or anion is surrounded by about three HFC-32 or two HFC-125.

The distributions of the HFC and anion surrounding the cation were visualized in terms of SDF and shown in Figure 10 for pure IL and HFC/IL binary mixtures. As shown in the figure, the anion tends to localize around the C_2, C_4, and C_5 atoms of the cation, while the HFC molecules find the interstices above and below the ring to fill in (see Figure 1 for definitions of atom labels). Similar behavior is observed for all the binary systems with the anion cloud slightly varying in terms of shape and area. Overall, with the addition of HFC, the distribution of the anions surrounding the cations is almost unaffected, consistent with the RDF and CN results shown in Figure 9.

Partial RDF. To further study the interaction between HFC and the ILs, the partial RDFs between specific interaction sites were calculated. Figure 11 depicts the partial RDFs of HFC-32 (left) and HFC-125 (right) in the binary systems with ILs at the lowest HFC mole fraction 0.071. The terminal carbon of the cation alkyl chain (C_t), central atom of the anion (an.), C of HFC-32, and C_1 of HFC-125 were considered in this analysis. Interactions with the C_2 atom of HFC-125 show similar or weaker structure than that to C_1, as shown in Figure S2. Interactions between HFCs and C_2, C_4, and C_5 of cations are shown in Figure S3, which are much weaker than that between HFC and C_t. The atom labels are provided in Figure 1. As shown in Figure 11, the C_t–C and C_t–C_1 RDFs are similar in all HFC/IL binary mixtures except for the slightly

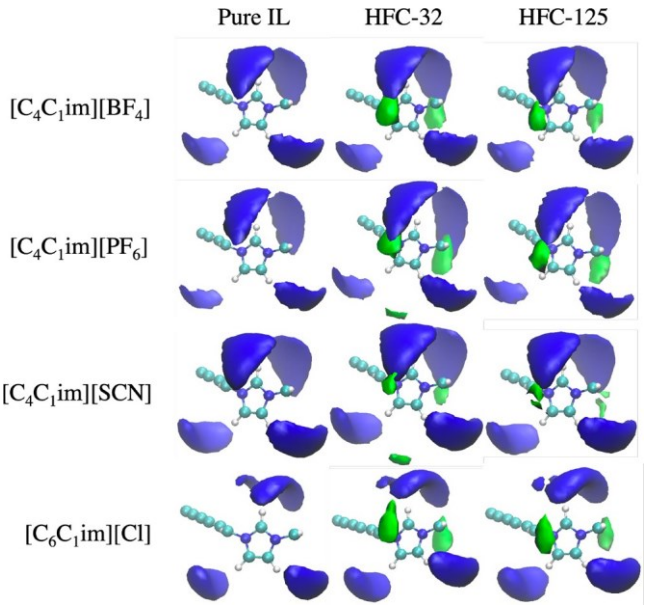

Figure 10. Calculated SDFs of pure IL at 300 K (except for pure [C_6C_1im][Cl] at 350 K), and the binary mixtures of HFC-32 and HFC-125 in IL mixtures at the highest HFC mole fraction as documented in Table 1. Central molecule is the cation. The blue cloud refers to the distribution of anion, and the green cloud represents the distribution of HFCs. The isodensity surface was chosen to be 40 and 80% of the maximum probability for anions and HFCs, respectively.

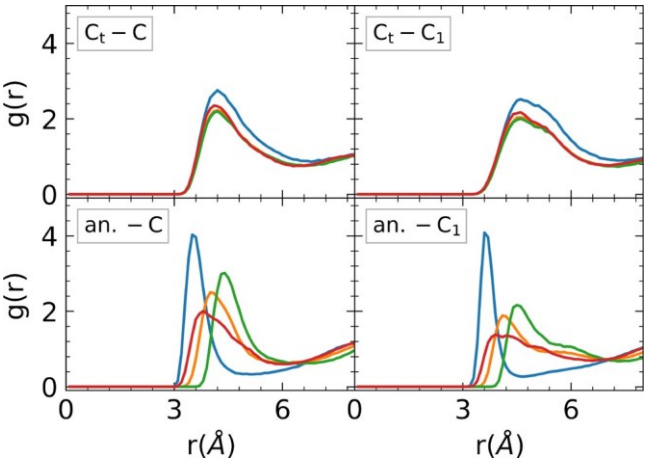

Figure 11. Partial RDFs of HFC-32 (left) and HFC-125 (right) in [C_4C_1im][BF_4] (orange), [C_4C_1im][PF_6] (green), [C_4C_1im][SCN] (red), and [C_6C_1im][Cl] (blue) at the lowest HFC mole fraction 0.071. The atom labels are shown in Figure 1. The central atom of the anion (an.) was used in the analysis.

higher intensity between 4 and 6 Å in the mixture with [C_6C_1im][Cl] for both HFC-32 and HFC-125. On the other hand, the first peak for an.-C and an.-C_1 interactions are higher and sharper in [C_6C_1im][Cl] mixtures than that in other ILs. The peak positions also appear at a shorter distance due to the smaller size of [Cl] relative to that of other anions. For the other three ILs, the peak position follows the size of the anion [PF_6] > [BF_4] > [SCN]. The an.–C and an.–C_1 interactions in [C_4C_1im][SCN] present the lowest peak height, indicating that [SCN] does not interact with HFCs as strongly as the other anions. This result is consistent with previous experi-

https://doi.org/10.1021/acs.jpcb.2c05787
J. Phys. Chem. B 2022, 126, 8309–8321

ment[26] which found that [C_4C_1im][SCN] has low molar solubility for HFC-32 and HFC-125.

To understand the solubility difference of HFC-32 and HFC-125 in different ILs, the near-azeotropic mixture HFC-410A was studied in the four ILs. The mole fractions of 0.177 for HFC-410A with 0.1235 mol % HFC-32 and 0.0535 mol % HFC-125 (a 50:50 wt % mixture of HFC-32 and HFC-125) were considered. The simulated density, relative excess volume, and self-diffusion coefficients of the ternary mixtures are documented in Tables S13 and S14. The densities of these ternary systems follow the same order as that of pure ILs: [C_4C_1im][PF_6] > [C_4C_1im][BF_4] > [C_4C_1im][SCN] > [C_6C_1im][Cl]. The calculated partial RDFs are shown in Figure 12, which are similar to those in the binary mixtures

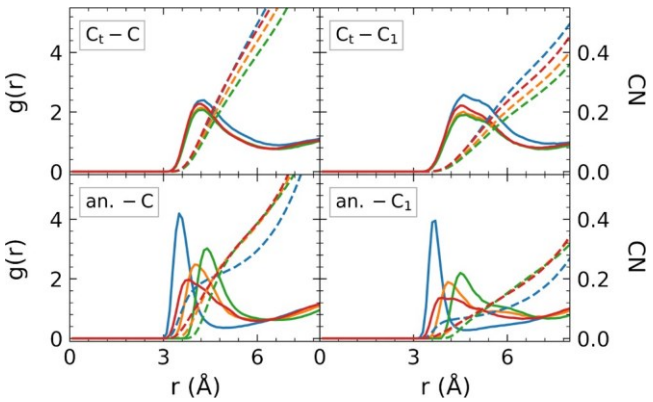

Figure 12. Calculated partial RDFs for the mixtures of HFC-410A in [C_4C_1im][BF_4] (orange), [C_4C_1im][PF_6] (green), [C_4C_1im][SCN] (red), and [C_6C_1im][Cl] (blue) and the corresponding coordination numbers (dashed lines, right axis) at 298.2 K and 0.984 atm.

shown in Figure 11, indicating that the addition of the second HFC at this concentration does not significantly affect the liquid structure established in the HFC/IL binary systems. The corresponding CNs were also calculated for each interaction and included in Figure 12. The CNs in the first solvation shell and the corresponding uncertainty estimated from block average are summarized in Table 2. The cutoff distance defining the first solvation shell was determined as the distance of the first minimum between the first two maxima in the corresponding RDF, which is 7.3 Å for both C_t–C and C_t–C_1 interactions in all ILs and 5.9, 6.2, 6.0, and 4.9 Å for an.–C and an.–C_1 interactions in [C_4C_1im][BF_4], [C_4C_1im][PF_6], [C_4C_1im][SCN], and [C_6C_1im][Cl], respectively.

Table 2. Coordination Number in the First Solvation Shell Calculated for the HFC-410A and IL Mixtures[a]

IL	[C_4C_1im][BF_4]	[C_4C_1im][PF_6]	[C_4C_1im][SCN]	[C_6C_1im][Cl]
		Cation–HFC		
CN_{C_t-C}	0.691_2	0.617_7	0.742_3	0.76_1
$CN_{C_t-C_1}$	0.322_8	0.284_1	0.357_4	0.41_1
$\Delta CN_{cat.}$	0.023_8	0.017_3	0.035_4	0.08_1
		Anion-HFC		
$CN_{an.-C}$	0.368_1	0.410_3	0.388_1	0.222_2
$CN_{an.-C_1}$	0.143_1	0.170_1	0.148_4	0.072_1
$\Delta CN_{an.}$	-0.016_1	-0.008_2	-0.020_4	-0.024_1

[a]The subscript is the uncertainty in the last digit which was estimated from block average, and the uncertainties for $\Delta CN_{cat.}$ and $\Delta CN_{an.}$ were calculated according to rules of error propagation.

For the ILs with the same cation ([C_4C_1im][BF_4], [C_4C_1im][PF_6], and [C_4C_1im][SCN]), the anions have an effect on the liquid structure. In [C_4C_1im][SCN], both CN_{C_t-C} and $CN_{C_t-C_1}$ are larger than those in [C_4C_1im][BF_4] and [C_4C_1im][PF_6], whereas both $CN_{an.-C}$ and $CN_{an.-C_1}$ are smaller than those in [C_4C_1im][PF_6] but similar to those in [C_4C_1im][BF_4]. The normalized coordination number difference

$$\Delta CN_{cat.} = CN_{C_t-C_1} - CN_{C_t-C} \times \frac{n_{HFC-125}}{n_{HFC-32}}$$

is positive and slightly larger for [C_4C_1im][SCN] than for the other two ILs, suggesting a slightly more favorable interaction of the HFC-125 with the cation terminal carbon than that of HFC-32. In contrast, the normalized coordination number difference

$$\Delta CN_{an.} = CN_{an.-C_1} - CN_{an.-C} \times \frac{n_{HFC-125}}{n_{HFC-32}}$$

was found to be lower (more negative) in [C_4C_1im][SCN] than in the other two ILs. The fact that $\Delta CN_{an.}$ is negative indicates that HFC-32 has slightly more preference than HFC-125 to interact with [SCN] anions. When comparing [C_6C_1im][Cl] with the other three ILs, both CN_{C_t-C} and $CN_{C_t-C_1}$ are larger, suggesting enhanced C_t–HFC interactions in [C_6C_1im][Cl]. However, both $CN_{an.-C}$ and $CN_{an.-C_1}$ are smaller in [C_6C_1im][Cl] than in the other ILs, which could be related to the shorter cutoff distance due to the smaller size of [Cl] compared to other anions. In all four ILs, $\Delta CN_{cat.}$ was found to be positive, and $\Delta CN_{an.}$was found to be negative, suggesting that the cation and anion have opposite selectivity. The cation favors HFC-125 over HFC-32, whereas the anion favors HFC-32 over HFC-125. In a previous experimental study,[26] it was found that HFC-32 and HFC-125 present different solubility in these four ILs. The analyses carried out in the current work suggests that the solubility differences observed in the ILs are due to differences in the ways in which the two HFCs interact with cations and anions. The larger HFC-125 tends to associate with the nonpolar alkyl tails of the cation, while HFC-32 prefers the more polar regions of the IL. This is consistent with the fact that HFC-32 has a significantly higher dielectric constant than HFC-125.

CONCLUSIONS

Experimental studies and MD simulations were carried out to study the thermodynamic, transport, and liquid solvation structure properties of HFC-32 and HFC-125 in ionic liquids. Reasonable agreement was observed for HFC-32 and HFC-125 in [C_4C_1im][BF_4] between simulations and experiments, suggesting the applied force fields are reliable. Simulations were then extended to include HFCs in [C_4C_1im][PF_6], [C_4C_1im][SCN], and [C_6C_1im][Cl]. The reliability of the force fields was validated against experimental density and dynamics of the pure ILs. It was found that adding HFCs to these ILs results in a smaller volume change compared with ideal mixing assumption. However, the packing structure of the IL, as characterized by COM and partial RDFs, was almost unaffected by the HFCs in the studied HFC concentration range. Faster dynamics of all species was observed with

https://doi.org/10.1021/acs.jpcb.2c05787
J. Phys. Chem. B 2022, 126, 8309–8321

increasing HFC concentrations in the mixtures. HFCs were found to diffuse much faster than the cation or the anion of the ILs. Detailed RDF and CN analyses suggested that both anion and cation affect HFC solubility, and the overall selectivity is likely related to differences in the way in which the two HFCs interact with the cation and anion. This study sheds light on the understanding of the HFC-32 and HFC-125 solubility and selectivity in different ILs at the molecular level and helps provide additional data and insight that can be used to design new ILs to separate HFC mixtures.

ASSOCIATED CONTENT

Supporting Information

The Supporting Information is available free of charge at https://pubs.acs.org/doi/10.1021/acs.jpcb.2c05787.

Force field parameters; numerical values of density, isobaric expansivity, isothermal compressibility, self-diffusivity, and shear viscosity; COM and partial RDF plots (PDF)

AUTHOR INFORMATION

Corresponding Author

Edward J. Maginn – *Department of Chemical and Biomolecular Engineering, University of Notre Dame, Notre Dame, Indiana 46556, United States*; orcid.org/0000-0002-6309-1347; Email: ed@nd.edu

Authors

Ning Wang – *Department of Chemical and Biomolecular Engineering, University of Notre Dame, Notre Dame, Indiana 46556, United States*; orcid.org/0000-0002-5515-6198

Yong Zhang – *Department of Chemical and Biomolecular Engineering, University of Notre Dame, Notre Dame, Indiana 46556, United States*; orcid.org/0000-0003-3988-5961

Karim S. Al-Barghouti – *Department of Chemical and Petroleum Engineering, University of Kansas, Lawrence, Kansas 66045, United States; Center for Environmentally Beneficial Catalysis, University of Kansas, Lawrence, Kansas 66047, United States; Institute for Sustainable Engineering, University of Kansas, Lawrence, Kansas 66045, United States*

Rajkumar Kore – *Department of Chemical and Petroleum Engineering, University of Kansas, Lawrence, Kansas 66045, United States; Center for Environmentally Beneficial Catalysis, University of Kansas, Lawrence, Kansas 66047, United States; Institute for Sustainable Engineering, University of Kansas, Lawrence, Kansas 66045, United States*; orcid.org/0000-0002-3361-1188

Aaron M. Scurto – *Department of Chemical and Petroleum Engineering, University of Kansas, Lawrence, Kansas 66045, United States; Center for Environmentally Beneficial Catalysis, University of Kansas, Lawrence, Kansas 66047, United States; Institute for Sustainable Engineering, University of Kansas, Lawrence, Kansas 66045, United States*; orcid.org/0000-0001-7214-1871

Complete contact information is available at: https://pubs.acs.org/10.1021/acs.jpcb.2c05787

Notes

The authors declare no competing financial interest.

ACKNOWLEDGMENTS

Support for this project was provided by the National Science Foundation, EFRI DChem: Next-generation Low Global Warming Refrigerants, Award no. EFRI-2029354. Computational resources were provided by and the Center for Research Computing (CRC) at the University of Notre Dame. We thank Professor Mark Shiflett and his group at the University of Kansas for helpful discussion.

REFERENCES

(1) Refrigerants environmental data. Ozone depletion and global warming potential. *Linde Gases AG*. https://www.linde-gas.com/en/images/Refrigerants%20environmental%20GWPs_74671_tcm17-111483.pdf (accessed Sep 20, 2022).

(2) Heath, E. A. Amendment to the Montreal protocol on substances that deplete the ozone layer (Kigali Amendment). *Int. Leg. Mater.* 2017, *56*, 193–205.

(3) Voigt, A.A global conversation about refrigerant regulations, reductions*ASHRAE J.*. 2021, *63*.8

(4) Welton, T. Room-temperature ionic liquidsRoom-temperature ionic liquids. Solvents for synthesis and catalysis. *Chem. Rev.* 1999, *99*, 2071–2084.

(5) Wasserscheid, P.; Welton, T.*Ionic Liquids in Synthesis*; Wiley Online Library, 2008; Vol. *1*.

(6) Marsh, K. N.; Boxall, J. A.; Lichtenthaler, R. Room temperature ionic liquids and their mixtures—a review. *Fluid Phase Equilib.* 2004, *219*, 93–98.

(7) Seiler, M.; Jork, C.; Kavarnou, A.; Arlt, W.; Hirsch, R. Separation of azeotropic mixtures using hyperbranched polymers or ionic liquids. *AIChE J.* 2004, *50*, 2439–2454.

(8) Shiflett, M. B.; Harmer, M. A.; Junk, C. P.; Yokozeki, A. Solubility and diffusivity of difluoromethane in room-temperature ionic liquids. *J. Chem. Eng. Data* 2006, *51*, 483–495.

(9) Shiflett, M. B.; Yokozeki, A. Vapor-liquid-liquid equilibria of pentafluoroethane and ionic liquid [bmim][PF_6] mixtures studied with the volumetric method. *J. Phys. Chem. B* 2006, *110*, 14436–14443.

(10) Shiflett, M. B.; Yokozeki, A. Solubility and diffusivity of hydrofluorocarbons in room-temperature ionic liquids. *AIChE J.* 2006, *52*, 1205–1219.

(11) Shiflett, M.; Yokozeki, A. Separation of difluoromethane and pentafluoroethane by extractive distillation using ionic liquid. *Chim. Oggi* 2006, *24*, 28–30.

(12) Lepre, L. F.; Andre, D.; Denis-Quanquin, S.; Gautier, A.; Pádua, A. A.; Costa Gomes, M. Ionic liquids can enable the recycling of fluorinated greenhouse gases. *ACS Sustainable Chem. Eng.* 2019, *7*, 16900–16906.

(13) Dong, L.; Zheng, D.; Sun, G.; Wu, X. Vapor-liquid equilibrium measurements of difluoromethane+[Emim] OTf, difluoromethane +[Bmim] OTf, difluoroethane+[Emim] OTf, and difluoroethane +[Bmim] OTf systems. *J. Chem. Eng. Data* 2011, *56*, 3663–3668.

(14) Sosa, J. E.; Ribeiro, R. P.; Castro, P. J.; Mota, J. P.; Araújo, J. M.; Pereiro, A. B. Absorption of fluorinated greenhouse gases using fluorinated ionic liquids. *Ind. Eng. Chem. Res.* 2019, *58*, 20769–20778.

(15) Higashi, B. S.; Takada, A. Molecular dynamics study of liquid CH_2F_2 (HFC-32). *Mol. Phys.* 1997, *92*, 641–650.

(16) Lisal, M.; Vacek, V. Effective potentials for liquid simulation of the alternative refrigerants HFC-134a (CF_3CH_2F) and HFC-125 (CF_3CHF_2). *Fluid Phase Equilib.* 1997, *127*, 83–102.

(17) Raabe, G. Molecular simulation studies on the vapor-liquid phase equilibria of binary mixtures of R-1234yf and R-1234ze (E) with R-32 and CO_2. *J. Chem. Eng. Data* 2013, *58*, 1867–1873.

(18) Budinskỳ, R.; Vacek, V.; Lısal, M. Vapor-liquid equilibria of alternative refrigerants and their binaries by molecular simulations employing the reaction Gibbs ensemble Monte Carlo method. *Fluid Phase Equilib.* 2004, *222*, 213–220.

(19) Alam, M. S.; Jeong, J. H. Thermodynamic properties and critical parameters of HFO-1123 and its binary blends with HFC-32

and HFC-134a using molecular simulations. *Int. J. Refrig.* 2019, *104*, 311−320.
(20) Morrow, T. I.; Maginn, E. J. Molecular dynamics study of the ionic liquid 1-n-butyl-3-methylimidazolium hexafluorophosphate. *J. Phys. Chem. B* 2002, *106*, 12807−12813.
(21) Sprenger, K.; Jaeger, V. W.; Pfaendtner, J. The general AMBER force field (GAFF) can accurately predict thermodynamic and transport properties of many ionic liquids. *J. Phys. Chem. B* 2015, *119*, 5882−5895.
(22) Raabe, G.; Köhler, J. Thermodynamical and structural properties of imidazolium based ionic liquids from molecular simulation. *J. Chem. Phys.* 2008, *128*, 154509.
(23) Annapureddy, H. V.; Kashyap, H. K.; De Biase, P. M.; Margulis, C. J. What is the origin of the prepeak in the x-ray scattering of imidazolium-based room-temperature ionic liquids? *J. Phys. Chem. B* 2010, *114*, 16838−16846.
(24) Gupta, K. M.; Jiang, J. Systematic investigation of nitrile based ionic liquids for CO_2 capture: A combination of molecular simulation and ab initio calculation. *J. Phys. Chem. C* 2014, *118*, 3110−3118.
(25) Asensio-Delgado, S.; Jovell, D.; Zarca, G.; Urtiaga, A.; Llovell, F. Thermodynamic and process modeling of the recovery of R410A compounds with ionic liquids. *Int. J. Refrig.* 2020, *118*, 365−375.
(26) Morais, A. R. C.; Harders, A. N.; Baca, K. R.; Olsen, G. M.; Befort, B. J.; Dowling, A. W.; Maginn, E. J.; Shiflett, M. B. Phase equilibria, diffusivities, and equation of state modeling of HFC-32 and HFC-125 in imidazolium-based ionic liquids for the separation of R-410A. *Ind. Eng. Chem. Res.* 2020, *59*, 18222−18235.
(27) Wang, J.; Wolf, R. M.; Caldwell, J. W.; Kollman, P. A.; Case, D. A. Development and testing of a general amber force field. *J. Comput. Chem.* 2004, *25*, 1157−1174.
(28) de Andrade, J.; Böes, E. S.; Stassen, H. Computational study of room temperature molten salts composed by 1-alkyl-3-methylimidazolium cations - force-field proposal and validation. *J. Phys. Chem. B* 2002, *106*, 13344−13351.
(29) Liu, Z.; Huang, S.; Wang, W. A refined force field for molecular simulation of imidazolium-based ionic liquids. *J. Phys. Chem. B* 2004, *108*, 12978−12989.
(30) Doherty, B.; Zhong, X.; Gathiaka, S.; Li, B.; Acevedo, O. Revisiting OPLS force field parameters for ionic liquid simulations. *J. Chem. Theory Comput.* 2017, *13*, 6131−6145.
(31) Frisch, M. J.; Trucks, G. W.; Schlegel, H. B.; Scuseria, G. E.; Robb, M. A.; Cheeseman, J. R.; Scalmani, G.; Barone, V.; Petersson, G. A.; Nakatsuji, H.; Li, X.; Caricato, M.; Marenich, A. V.; Bloino, J.; Janesko, B. G.; Gomperts, R.; Mennucci, B.; Hratchian, H. P.; Ortiz, J. V.; Izmaylov, A. F.; Sonnenberg, J. L.; Williams-Young, D.; Ding, F.; Lipparini, F.; Egidi, F.; Goings, J.; Peng, B.; Petrone, A.; Henderson, T.; Ranasinghe, D.; Zakrzewski, V. G.; Gao, J.; Rega, N.; Zheng, G.; Liang, W.; Hada, M.; Ehara, M.; Toyota, K.; Fukuda, R.; Hasegawa, J.; Ishida, M.; Nakajima, T.; Honda, Y.; Kitao, O.; Nakai, H.; Vreven, T.; Throssell, K.; Montgomery, J. A., Jr.; Peralta, J. E.; Ogliaro, F.; Bearpark, M.; Heyd, J. J.; Brothers, E. N.; Kudin, K. N.; Staroverov, V. N.; Kobayashi, R.; Normand, J.; Raghavachari, K.; Rendell, A.; Burant, J. C.; Iyengar, S. S.; Tomasi, J.; Cossi, M.; Millam, J. M.; Klene, M.; Adamo, C.; Cammi, R.; Ochterski, J. W.; Martin, R. L.; Morokuma, K.; Farkas, O.; Foresman, J. B.; Fox, D. J.*Gaussian 16*, revision C.01; Gaussian, Inc.: Wallingford, CT, 2016.
(32) Bayly, C. I.; Cieplak, P.; Cornell, W.; Kollman, P. A. A well-behaved electrostatic potential based method using charge restraints for deriving atomic charges: the RESP model. *J. Phys. Chem.* 1993, *97*, 10269−10280.
(33) Zhang, Y.; Maginn, E. J. A simple AIMD approach to derive atomic charges for condensed phase simulation of ionic liquids. *J. Phys. Chem. B* 2012, *116*, 10036−10048.
(34) Befort, B. J.; DeFever, R. S.; Tow, G. M.; Dowling, A. W.; Maginn, E. J. Machine learning directed optimization of classical molecular modeling force fields. *J. Chem. Inf. Model.* 2021, *61*, 4400−4414.
(35) Plimpton, S. Fast parallel algorithms for short-range molecular dynamics. *J. Comput. Phys.* 1995, *117*, 1−19.
(36) Thompson, A. P.; Aktulga, H. M.; Berger, R.; Bolintineanu, D. S.; Brown, W. M.; Crozier, P. S.; in 't Veld, P. J.; Kohlmeyer, A.; Moore, S. G.; Nguyen, T. D.; et al. LAMMPS - a flexible simulation tool for particle-based materials modeling at the atomic, meso, and continuum scales. *Comput. Phys. Commun.* 2022, *271*, 108171.
(37) Martínez, J. M.; Martínez, L. Packing optimization for automated generation of complex system's initial configurations for molecular dynamics and docking. *J. Comput. Chem.* 2003, *24*, 819−825.
(38) Martínez, L.; Andrade, R.; Birgin, E. G.; Martínez, J. M. PACKMOL: A package for building initial configurations for molecular dynamics simulations. *J. Comput. Chem.* 2009, *30*, 2157−2164.
(39) Ewald, P. P. Die Berechnung optischer und elektrostatischer Gitterpotentiale. *Ann. Phys. (Berlin, Ger.)* 1921, *369*, 253−287.
(40) Hockney, R.; Eastwood, J.*Computer Simulation Using Particles*; Taylor & Francis, 1988.
(41) Hoover, W. G. Canonical dynamics: Equilibrium phase-space distributions. *Phys. Rev. A* 1985, *31*, 1695.
(42) Shinoda, W.; Shiga, M.; Mikami, M. Rapid estimation of elastic constants by molecular dynamics simulation under constant stress. *Phys. Rev. B* 2004, *69*, 134103.
(43) Leach, A.*Molecular Modelling: Principles and Applications*; Prentice Hall, 2001.
(44) Allen, M.; Tildesley, D.*Computer Simulation of Liquids*; Oxford University Press, 2017.
(45) Humbert, M. T.; Zhang, Y.; Maginn, E. J. PyLAT: Python LAMMPS analysis tools. *J. Chem. Inf. Model.* 2019, *59*, 1301−1305.
(46) Yeh, I.-C.; Hummer, G. System-size dependence of diffusion coefficients and viscosities from molecular dynamics simulations with periodic boundary conditions. *J. Phys. Chem. B* 2004, *108*, 15873−15879.
(47) Zhang, Y.; Otani, A.; Maginn, E. J. Reliable viscosity calculation from equilibrium molecular dynamics simulations: A time decomposition method. *J. Chem. Theory Comput.* 2015, *11*, 3537−3546.
(48) Zhang, Y.; Zhang, Y.; McCready, M. J.; Maginn, E. J. Evaluation and refinement of the general AMBER Force Field for nineteen pure organic electrolyte solvents. *J. Chem. Eng. Data* 2018, *63*, 3488−3502.
(49) Bird, R.; Stewart, W.; Lightfoot, E.*Transport Phenomena*; Wiley, 2006; vol. *1*.
(50) Ahosseini, A.; Scurto, A. M. Viscosity of imidazolium-based ionic liquids at elevated pressures: cation and anion effects. *Int. J. Thermophys.* 2008, *29*, 1222−1243.
(51) Morais, A. R. C.; Simoni, L. D.; Shiflett, M. B.; Scurto, A. M. Viscosity and density of a polyol ester lubricating oil saturated with compressed hydrofluoroolefin refrigerants. *J. Chem. Eng. Data* 2020, *65*, 4335−4346.
(52) Ahosseini, A.; Ren, W.; Weatherley, L. R.; Scurto, A. M. Viscosity and self-diffusivity of ionic liquids with compressed hydrofluorocarbons: 1-Hexyl-3-methyl-imidazolium bis-(trifluoromethylsulfonyl)amide and 1,1,1,2-tetrafluoroethane. *Fluid Phase Equilib.* 2017, *437*, 34−42.
(53) Price, W. S. Pulsed-field gradient nuclear magnetic resonance as a tool for studying translational diffusion: Part 1. Basic theory. *Concepts Magn. Reson.* 1997, *9*, 299−336.
(54) Price, W. S. Pulsed-field gradient nuclear magnetic resonance as a tool for studying translational diffusion: Part II. Experimental aspects. *Concepts Magn. Reson.* 1998, *10*, 197−237.
(55) Schleicher, J.Kinetics and Solvent Effects in the Synthesis of Ionic Liquids. MS thesis, University of Kansas, 2007. http://hdl.handle.net/1808/32095.
(56) Matkowska, D.; Hofman, T. High-pressure volumetric properties of ionic liquids: 1-butyl-3-methylimidazolium tetrafluoroborate,$[C_4mim][BF_4]$, 1-butyl-3-methylimidazolium methylsulfate $[C_4mim][MeSO_4]$ and 1-ethyl-3-methylimidazolium ethylsulfate, $[C_2mim][EtSO_4]$. *J. Mol. Liq.* 2012, *165*, 161−167.
(57) Tomida, D.; Kenmochi, S.; Qiao, K.; Yokoyama, C. Densities and thermal conductivities of ionic liquids, 1-hexyl-3-methylimidazolium chloride, 1-octyl-3-methylimidazolium chloride, and 1-octyl-3-

methylimidazolium bromide, at pressures up to 20 MPa. *High Temp. - High Pressures* 2017, *46*, 101−114.
(58) Safarov, J.; Suleymanli, K.; Aliyev, A.; Yeadon, D. J.; Jacquemin, J.; Bashirov, M.; Hassel, E. p, ρ, T) data of 1-butyl-3-methylimidazolium hexafluorophosphate. *J. Chem. Thermodyn.* 2020, *141*, 105954.
(59) Królikowska, M.; Hofman, T. Densities, isobaric expansivities and isothermal compressibilities of the thiocyanate-based ionic liquids at temperatures (298.15−338.15 K) and pressures up to 10 MPa. *Thermochim. Acta* 2012, *530*, 1−6.
(60) Tokuda, H.; Tsuzuki, S.; Susan, M. A. B. H.; Hayamizu, K.; Watanabe, M. How ionic are room-temperature ionic liquids? An indicator of the physicochemical properties. *J. Phys. Chem. B* 2006, *110*, 19593−19600.
(61) Lemmon, E. W.; Bell, I. H.; Huber, M. L.; McLinden, M. O.*NIST Standard Reference Database 23: Reference Fluid Thermodynamic and Transport Properties-REFPROP*, version 10.0; National Institute of Standards and Technology, Standard Reference Data Program: Gaithersburg, MD, 2018. https://www.nist.gov/srd/refprop.
(62) Lemmon, E. W.; Jacobsen, R. T. A new functional form and new fitting techniques for equations of state with application to pentafluoroethane (HFC-125). *J. Phys. Chem. Ref. Data* 2005, *34*, 69−108.
(63) Matkowska, D.; Hofman, T. High-pressure volumetric properties of ionic liquids: 1-butyl-3-methylimidazolium tetrafluoroborate, [C_4mim][BF_4], 1-butyl-3-methylimidazolium methylsulfate [C_4mim][$MeSO_4$] and 1-ethyl-3-methylimidazolium ethylsulfate, [C_2mim][$EtSO_4$]. *J. Mol. Liq.* 2012, *165*, 161−167.
(64) Tokuda, H.; Hayamizu, K.; Ishii, K.; Susan, M. A. B. H.; Watanabe, M. Physicochemical properties and structures of room temperature ionic liquids. 1. Variation of anionic species. *J. Phys. Chem. B* 2004, *108*, 16593−16600.
(65) Ahosseini, A.; Ortega, E.; Sensenich, B.; Scurto, A. M. Viscosity of n-alkyl-3-methyl-imidazolium bis(trifluoromethylsulfonyl)amide ionic liquids saturated with compressed CO_2. *Fluid Phase Equilib.* 2009, *286*, 72−78.
(66) Zhang, Y.; Wang, X.; Yin, J. Viscosity of saturated mixtures of 1-hexyl-3-methyl-imidazolium bis(trifluoromethylsulfonyl)amide with R600a and R152a. *J. Chem. Thermodyn.* 2020, *141*, 105970.
(67) Zhang, Y.; Jia, X.; Wang, X. Experimental investigation on the viscosity of [Hmim][Tf_2N] saturated with R1234ze(E) or R1234yf. *Int. J. Refrig.* 2020, *117*, 338−345.
(68) Tomida, D.; Kumagai, A.; Qiao, K.; Yokoyama, C. Viscosity of 1-butyl-3-methylimidazolium tetrafluoroborate + CO_2 mixture. *High Temp. - High Pressures* 2008, *37*, 81−89.
(69) Kelkar, M. S.; Maginn, E. J. Effect of temperature and water content on the shear viscosity of the ionic liquid 1-ethyl-3-methylimidazolium bis(trifluoromethanesulfonyl)imide as studied by atomistic simulations. *J. Phys. Chem. B* 2007, *111*, 4867−4876.

https://doi.org/10.1021/acs.jpcb.2c05787
J. Phys. Chem. B 2022, 126, 8309−8321